Physica Medica 128 (2024) 104850

Contents lists available at ScienceDirect

Physica Medica

journal homepage: www.elsevier.com/locate/ejmp

Original paper

Validation of Light–Ion Quantum Molecular Dynamics (LIQMD) model for hadron therapy

Yoshi-hide Sato [a], Dousatsu Sakata [b,c,d], David Bolst [c], Edward C. Simpson [e], Andrew Chacon [c,f], Mitra Safavi-Naeini [c,f,g], Susanna Guatelli [c], Akihiro Haga [a,*]

[a] Department of Biological Sciences, Tokushima University, Tokushima 770-8503, Japan
[b] Division of Health Sciences, Graduate School of Medicine, Osaka University, Osaka 565-0871, Japan
[c] Centre For Medical and Radiation Physics, University of Wollongong, Wollongong NSW 2522, Australia
[d] School of Physics, University of Bristol, Bristol, BS8 1TL, United Kingdom
[e] Department of Nuclear Physics and Accelerator Applications, Research School of Physics, The Australian National University, Canberra, ACT 2601, Australia
[f] Australian Nuclear Science and Technology Organisation (ANSTO), NSW, Australia
[g] Brain and Mind Centre, University of Sydney, Sydney, NSW, Australia

ARTICLE INFO

Keywords:
Quantum Molecular Dynamics
Geant4
Fragmentation
In-vivo Positron Emission Tomography
Cross-section

ABSTRACT

Purpose: This study aims to validate the Light-Ion Quantum Molecular Dynamics (LIQMD) model, an advanced version of the QMD model for more accurate simulations in hadron therapy, incorporated into Geant4 (release 11.2).

Methods: Two sets of experiments are employed. The first includes positron-emitter distributions along the beam path for 350 MeV/u ^{12}C ions incident on a PMMA target, obtained from in–vivo Positron Emission Tomography (PET) experiments at QST (Chiba, Japan). The second comprises cross-sections for 95 MeV/u ^{12}C ions incident on thin targets (H, C, O, Al, and Ti), obtained from experiments at GANIL (Caen, France). The LIQMD model's performance is compared with the experimental data and the default QMD model results.

Results: The LIQMD model can predict the profile shape of positron-emitting radionuclide yields with better accuracy than the default QMD model, although some discrepancies remains. The consistency observed in the production of positron-emitting radionuclides aligns with the thin target cross-section analysis. The LIQMD model significantly improves the differential and double-differential cross-sections of fragments produced in thin targets, especially in the forward direction. The overestimation of ^{10}C production in the in–vivo PET benchmark is consistent with the 95 MeV/u ^{12}C cross-section test. Overall, the LIQMD model demonstrates better agreement with experimental measurements for nearly all fragment species compared to the QMD model.

Conclusions: The LIQMD model offers an improved description of the fragmentation process in hadron therapy. Future work should involve further validation against additional experimental measurements to confirm these findings.

1. Introduction

Hadron therapy, such as carbon ion therapy, relies on accurate estimation of the biological dose, with nuclear fragmentation being a pivotal process in this determination. Monte Carlo (MC) simulations codes, including Geant4 [1–3], are used extensively to calculate the dose in the tumor target and surrounding regions. Therefore, their validation against experimental measurements is essential [4,5]. However, existing ion fragmentation models in Geant4, the Quantum Molecular Dynamics (QMD), Binary Intranuclear Cascade (BIC) [6], and Liège Intranuclear Cascade (INCL++) [7,8] models, have exhibited significant discrepancies with experimental data in previous studies (e.g., Refs. [9–11]). For example, Dudouet et al. [9] compared Geant4 (Geant4 ver. 9.2) results against experimental data when calculating fragment cross-sections in several targets (H, C, O, Al, and Ti) due to a carbon ion beam of about 95 MeV/u energy, and they found that the considered models, including BIC, INCL and QMD, did not accurately reproduce the data, neither in term of production rates nor for angular or energy distributions. Among BIC, QMD and INCL, the fragment energy distribution obtained with the QMD model provided a better agreement against the reference data, whereas it was noted that the angular distribution of the fragments in the QMD model (excluding proton fragment) had an

* Corresponding author.
E-mail addresses: dosatsu.sakata@cern.ch (D. Sakata), haga@tokushima-u.ac.jp (A. Haga).

https://doi.org/10.1016/j.ejmp.2024.104850
Received 15 May 2024; Received in revised form 11 September 2024; Accepted 24 October 2024
Available online 28 November 2024

unrealistic peak [9]. When considering later versions of Geant4 (ver. 10.2.2 and 10.2.3), the above three Geant4 fragmentation models have been benchmarked against experimental data in terms of yield of positron-emitting nuclides, for in–vivo Positron Emission Tomography (PET) applications [11]. Another study [10] benchmarked the emission yield, angular and kinetic energy distributions of light fragments produced by a 400 MeV/u carbon ion beam in a thick water (or water equivalent) phantom against experimental measurements. Both studies showed that there is room for improvement in the fragmentation models of Geant4.

When compared to the BIC and INCL models, the unique feature of the QMD model is the description of the dynamics of each participating nucleon of the target and of the projectile. This approach is based on the solution of the equation of motion in a many-body system with a self-consistent mean field potential. In a previous study, efforts were made to improve the QMD nuclear fragment reaction model implemented in Geant4, addressing the need for a more accurate description of fragment production, important for dosimetric calculations for carbon ion therapy [12]. This involved improving the nucleon–nucleon interaction, integrating the alpha-cluster formation in projectile/target nuclei, and optimizing the QMD model parameters. The resulting QMD model, named *Light-Ion QMD* (LIQMD) model, was recently released in Geant4 version 11.2. While the LIQMD has demonstrated an improved fragment production for a 400 MeV/u carbon ion beam in water, further validation is necessary for different application scenarios, including different targets and incident carbon ion energies, of interest for clinical applications.

To contribute to fill this knowledge gap, the aim of this study is to validate the LIQMD model when calculating the yield of positron-emitting radionuclides obtained with a 350 MeV/u ^{12}C ion beam incident on a PMMA target, as assessed by Chacon et al. [11,13]. In comparison to photon-based therapy, heavy-ion therapy minimizes radiation exposure to organs-at-risk (OAR) while ensuring adequate dose coverage of the target volume [14,15]. However, the precision of heavy-ion therapy amplifies its vulnerability to factors like patient positioning, anatomical changes, inaccuracies in stopping power ratio relative to water, and variations in beam energy [16,17]. These uncertainties in particle range pose significant challenges, necessitating a reliable method for verifying the projected range in patients. A practical method is PET imaging of positron emitters. In this method, positron emitters generated by fragmentation of projectile and target particles on the beam path can be imaged by PET [18,19] and actually applied in the measurement of positron-emitting radionuclides [11]. In this study, the reconstructed positron-emitting radionuclide's distribution was directly compared with that obtained from the LIQMD model.

While the comparison in terms of positron-emitting radionuclides yields provides validation of the LIQMD model in a practical situation of clinical application, it does not directly assess the accuracy of fragmentation due to the blurring in PET image caused by kinetic motion of the produced positron and other dynamic effects. Therefore, in this study, the total, differential, and double-differential cross-sections of 95 MeV/u ^{12}C ions in five elements (H, C, O, Al, and Ti) were also compared to experimental measurements [9] to offer information in terms of fundamental physics modelling when investigating the reason of eventual discrepancies between experimental data and simulation results.

2. Materials and methods

In this study, an extended QMD model for light ions, the LIQMD model, was evaluated for its effectiveness in the production of positron-emitting radionuclides, as well as the direct assessment of yields, differential, and double-differential cross-sections in fragmentation within the energy ranges pertinent to particle radiotherapy. This section first elucidates the distinctive features of the developed QMD model, followed by a detailed description of the experiments utilized in the current evaluation and the evaluation assessment methodology.

2.1. LIQMD model

The QMD model simulates the dynamics of all participating nucleons in inelastic nucleus–nucleus scattering using an Hamiltonian approach,

$$\dot{\boldsymbol{r}}_i = \frac{\partial H}{\partial \boldsymbol{p}_i}, \quad \dot{\boldsymbol{p}}_i = -\frac{\partial H}{\partial \boldsymbol{r}_i}, \tag{1}$$

where $\boldsymbol{r}_i$ and $\boldsymbol{p}_i$ denote the position and momentum vectors for the ith particle, respectively. The total energy (Hamiltonian H) has a Lorentz covariant form [20,21],

$$H = \sum_i \sqrt{\boldsymbol{p}_i^2 + m_i^2 + 2m_i V_i} \tag{2}$$

where V_i is the effective potential felt in the ith particle with mass m_i. While various nuclear models propose effective potentials, the LIQMD model employs the Skyrme interaction with the SkM* parameter set (see Ref. [12], for details) as the primary improvement. This choice accounts for well-described features of nuclear matter and finite nuclei. A previous study has demonstrated that SkM* adequately describes fragmentation in water phantoms [12].

The second improvement involves the preparation of the initial ground states of the colliding nuclei. In a typical QMD model, such as the one used in Geant4 (JAERI QMD model), the positions and momenta of the nucleons are initially sampled based on the nuclear density and the Fermi momentum of the projectile and target nuclei, respectively [22,23]. In the LIQMD model, however, the formation of a regular tetrahedron comprising two protons and two neutrons was introduced to establish an α-cluster structure in the initial positions of the nucleons for ^{12}C and ^{16}O, which contain 3 and 4 α-clusters, respectively. These positions and their momenta yield an initially unrealistic binding energy, which is adjusted by solving the damped equation of motion to ensure that the calculated binding energy aligns with the experimental value within 1 keV/nucleon [12,24]. The fine-tuned positions are then considered as the ground state nucleus, maintaining the α-cluster structure in part. It is important to note that the incorporation of the α-cluster structure in the current LIQMD model was limited to ^{12}C and ^{16}O nuclei.

The final improvement involved the optimization of the QMD model parameters. Within this enhancement, we focused on two parameters: the square of the Gaussian wave packet width, denoted as L[fm^2], and the threshold of the cluster radius, denoted as R[fm]. These parameters were identified as sensitive factors in the classification of nuclear clusters, crucial for fragment formation. Through optimization, these parameters were adjusted to align with measured fragment yields and their angular distributions in experiments involving 400 MeV/u ^{12}C ion beams with water targets, resulting in a SkM*-α-cluster model with $(L, R) = (1.26, 3.99)$. Notably, the value $L = 1.26$ was validated for light nuclei (with A $\sim$ 40) through charge radii analysis in the ground state nucleus. In the QMD model of Geant4, 2.0 [fm^2] is used as the default value of L, but this value overestimates the charge radii for light nuclei, yet adequately reproduces experimental results for heavy nuclei (such as ^{208}Pb). This trend is also true for the LIQMD model.

The incorporation of the α-cluster structure is specific to ^{12}C and ^{16}O, and the QMD model parameters L and R are optimized for the ^{12}C–ion – water reaction. As such, the optimized square of the Gaussian wave packet width, L, has been validated for light ions. Consequently, the LIQMD model is considered to effectively depict nucleus–nucleus collisions involving light ions (up to A $\sim$ 40). Validating or extending the LIQMD model to collisions with heavier nuclei remains a crucial area for future research. This study further validates the LIQMD model in different scenarios, including the experiments on positron-emitting radionuclides production and the thin-target experiments detailed below.

Table 1
Geant4 models used for the simulation of hadronic interactions.

Interaction	Projectile	Energy range	G4Model
Radioactive Decay	GenericIon	–	G4DecayPhysics G4RadioactiveDecayPhysics
Hadron Elastic	GenericIon	0–100 TeV/n	G4HadronElasticPhysicsHP
	d, t, ^{3}He, α	0–100 TeV/n	G4HadronElasticPhysicsLHEP
	p	0 – 100 TeV	G4ChipsElasticModel
	n	0–20 MeV 20 MeV–100 TeV	G4NeutronHPElastic G4ChipsElasticModel
Hadron Inelastic	GenericIon, d, t, ^{3}He, α	0 – 100 MeV/n 100 MeV/n–5.99 GeV/n 5.99 GeV/n–100 TeV/n	G4BinaryLightIonReaction G4QMDReaction FTFP
	p	0–3 GeV 3 GeV–12 GeV 12 GeV – 100 TeV	G4BinaryCascade FTFP QGSP
	n	0–20 MeV 20 MeV–6 GeV 6 GeV–25 GeV 25 GeV–100 TeV	G4NeutronHPInelastic G4BinaryCascade FTFP QGSP
Hadron Inelastic[a]	GenericIon, d, p, d, t, ^{3}He, α	0–30 MeV/n 30 MeV/n–5.99 GeV/n 5.99 GeV/n–100 TeV/n	G4BinaryLightIonReaction LIQMD FTFP
Fission	n	0–20 MeV 20 MeV–100 TeV	G4NeutronHPFission G4LFission
Capture	n	0–20 MeV 20 MeV–100 TeV	G4NeutronHPCapture G4nRadCapture

[a] This hadron inelastic was used in the LIQMD model simulations. The simulations for neutron inelastic reaction and others are the same as those for the QMD model simulation.

2.2. Comparison with experiments

In the present study, the performance of the LIQMD model was verified by using reconstruction data of positron-emitting radionuclide distribution in a PMMA target with an experiment conducted at QST [11], and cross-sections in thin targets with an experiment conducted at GANIL [25]. The former is important in the development of beam monitoring as a real time quality assurance of the particle therapy, while the latter gives more essential information about discrepancies between the experimental data and the simulation, including in positron-emitting radionuclide distribution.

2.2.1. Positron-emitting radionuclide production

The distribution of three positron-emitting radionuclides, ^{10}C, ^{11}C, and ^{15}O has been determined experimentally for carbon beams in Ref. [11], where the phantom was irradiated with a continuous periodic beam pulse (in spills). During and after beam irradiation, the positron annihilations caused by positron-emitting radionuclides were recorded by using a whole-body DOI–PET scanner prototype developed at QST [26], and then, reconstructed frame-by-frame using the 3D ordinary Poisson ordered-subset-expectation–maximization (3D-OP-OSEM) algorithm [27], with a voxel size of $1.5 \times 1.5 \times 1.5$ mm^3. Then, the time activity curve (TAC) analysis of positron annihilation was performed for each slice, which is a region around the beam axis with a width of 1.5 mm in the direction of the beam axis. The TAC after irradiation was fitted with,

$$A(t) = A_{0,C11}e^{-\lambda_{C11}t} + A_{0,C10}e^{-\lambda_{C10}t} + A_{0,O15}e^{-\lambda_{O15}t}, \quad (3)$$

where λ_{C11}, λ_{C10}, and λ_{O15} are the decay constants of ^{11}C, ^{10}C, and ^{15}O, respectively. The activities at $t = 0$ (the time at the end of spills), $A_{0,C11}$, $A_{0,C10}$, and $A_{0,O15}$, were determined by this fit.

A comparison with experiments using the Geant4 default QMD model, as well as the BIC and INCL models, was made in Ref. [11] using Geant4 version 10.2.3. In this study, we compare the results of the same test, obtained with the more recently developed LIQMD model and the default Geant4 QMD model, using Geant4 version 11.1.1. Geant4 models used for the simulation of hadronic interactions are summarized in Table 1. It is noted here that different physics constructors were employed for the LIQMD and QMD simulations. Specifically, the hadron inelastic employed in the LIQMD model simulation switches from QMD to BIC when the kinetic energy of the projectile is below 30 MeV/u, whereas the hadron inelastic used in the default QMD model simulation switches at 100 MeV/u.

Although the simulation can directly obtain information for each positron-emitting radionuclide, the yields were obtained through the analysis of TAC, as in the experiment. The experimental setup, such as the beam, was computationally reproduced in the simulation. See Ref. [11] for the specific settings. The only difference from the experiment is that no reconstruction is required. In other words, the positron position and the time of the positron annihilation event can be obtained directly within the framework of the simulation. The point spread function accompanying PET imaging was taken into account in the analysis phase. More concretely, we first obtained positron events from the MC simulation, and then, $A_{0,C11}(z)$, $A_{0,C10}(z)$, and $A_{0,O15}(z)$ as a function of the beam axis (denoted as z) were estimated by the TAC analysis. Finally the yield in z was calculated by

$$Y(z) = \frac{\tilde{A}_0(z)}{\lambda N_0}, \quad (4)$$

where, $\tilde{A}_0$ is the result of the convolution integral of A_0 with a Gaussian point spread kernel G, $(G * A_0)$, of the PET system (the full width at half maximum, 2.6 mm). A_0 and λ are the activity and decay constant of any of ^{10}C, ^{11}C, and ^{15}O, respectively. N_0 is the number of incident particles (10^8 in our simulation). Ten simulations with different random seeds were performed to obtain the mean and standard error of the yields.

The evaluation was performed with the mean absolute error (MAE),

$$MAE = \frac{1}{n}\sum_i^n |y_i - \hat{y}_i|, \quad (5)$$

where n is the number of data for each positron-emitting radionuclide production and $\hat{y}$ refers to its prediction. The experimental data is denoted as y. We chose the MAE as the metric to compare the two fragmentation models (default QMD and LIQMD).

2.2.2. Fragment yield, differential, and double-differential cross-sections calculated for a 95 MeV/u carbon ion beam incident on thin targets

Fragment production cross-section, differential cross-section (angular distribution), and double-differential cross-section (energy distribution for a specific angle) have been measured using a 95 MeV/u carbon ion beam incident on a target of C, CH_2, Ti, Al, Al_2O_3 and PMMA ($C_5H_8O_2$) at GANIL (Accélérateur National d'Ions Lourds) and documented in Ref. [25,28]. Seventeen fragments were studied: ^{1}H (4.0), ^{2}H (5.2), ^{3}H (6.1), ^{3}He (14.2), ^{4}He (16.0), ^{6}He (18.6), ^{6}Li (29.9), ^{7}Li (31.7), ^{7}Be (44.3), ^{9}Be (48.6), ^{10}Be (50.5), ^{8}B (60.6), ^{10}B (65.8), ^{11}B (68.1), ^{10}C (81.3), ^{11}C (84.2) and ^{12}C (86.9). The values in parentheses following each fragment species is the energy threshold (MeV) described in Ref. [9]. That is, particles below this energy were not counted in the yield analysis. In our simulation study, ^{1}H, ^{12}C, ^{16}O, ^{27}Al, and ^{48}Ti, which are the dominant isotopes, are used as targets.

Specifically,

$$\sigma = \sigma_R \frac{N}{N_0}, \tag{6}$$

$$\frac{d\sigma}{d\Omega} = \sigma_R \frac{\Delta N(\theta)}{N_0 \Delta\Omega(\theta)}, \tag{7}$$

$$\frac{d^2\sigma}{d\Omega dE} = \sigma_R \frac{\Delta N(\theta, E)}{N_0 \Delta\Omega(\theta)\Delta E}, \tag{8}$$

were used for calculating production cross-section, differential cross-section, and double-differential cross-section, respectively. Here, N, $\Delta N(\theta)$, and $\Delta N(\theta, E)$ are the total fragment yield, the fragment yield for solid angle $\Omega(\theta)$, and the fragment yield for solid angle $\Omega(\theta)$ and for energy range ΔE in the incident particle event N_0, respectively. The energy (E) here refers to the energy per nucleon. 10^7 particles have been simulated per run. Ten runs were performed to obtain the mean and standard error of the yields in each target. An angular discretization was set as 2 degrees as for the experimental data, whereas an energy discretization was set as 5 MeV in our evaluation. Notably, the QMD model simulates only inelastic collisions in Geant4; The QMD model runs until it determines that inelastic nucleus–nucleus scattering occurs in the simulation. Therefore, the inelastic cross-section (reaction cross-section σ_R) should be multiplied into the fragmentation result from the QMD model, in order to make the simulation results comparable with the experiment. For the total inelastic hadronic cross-section σ_R, the Glauber–Gribov model [29,30] is adopted. Again, the evaluation was performed with MAE,

$$MAE = \frac{1}{n}\sum_{i}^{n} |y_i - \hat{y}_i| \tag{9}$$

where n is the number of data for each cross-section of each target-fragment combination and $\hat{y}$ refers to one of the predicted total cross-section, differential cross-section, or double-differential cross-section, depending on the context. The experimental data is denoted as y.

While the in–vivo PET test is a useful benchmark of the LIQMD and default QMD models in a realistic application scenario of Geant4 in hadron therapy, this test allows to identify differences between the two fragmentation models when predicting fundamental physics quantities, that is, the cross-sections.

3. Result

3.1. Positron emitting radionuclide production

Fig. 1 displays the yield distribution of positron-emitting radionuclides along the beam direction in a PMMA phantom irradiated with 350 MeV/u ^{12}C ions, where each yield of the three positron-emitting radionuclides (^{11}C, ^{10}C, and ^{15}O) is depicted. A remarkable improvement can be observed in the prediction of ^{15}O yield, though the experimental error is relatively larger when compared to the other positron-emitting radionuclides. For comparison, normalized yields to the mean yield at the entrance of the plateau region (100-130 mm) are also shown in the Appendix, where it becomes apparent that the LIQMD model reproduces the experimental data very well.

Table 2
Mean absolute error (MAE) of the positron-emitting radionuclides production (Fig. 1). The **bold** format indicates a smaller MAE, as provided by either the QMD or the LIQMD model.

Nuclide	QMD	LIQMD
^{11}C	$(1.38 \pm 0.04) \times 10^{-4}$	$\mathbf{(1.18 \pm 0.04) \times 10^{-4}}$
^{10}C	$\mathbf{(1.93 \pm 0.03) \times 10^{-5}}$	$(3.09 \pm 0.03) \times 10^{-5}$
^{15}O	$(2.91 \pm 0.14) \times 10^{-5}$	$\mathbf{(1.60 \pm 0.14) \times 10^{-5}}$

Table 3
Mean absolute error (MAE) of the total cross-sections of fragment production shown in Fig. 2. The **bold** format indicates a smaller MAE, as provided by either the QMD or LIQMD model.

Target	QMD	LIQMD
^{1}H	$(2.97 \pm 0.76) \times 10^{-2}$	$\mathbf{(2.44 \pm 0.76) \times 10^{-2}}$
^{12}C	$(1.15 \pm 0.24) \times 10^{-1}$	$\mathbf{(8.93 \pm 2.38) \times 10^{-2}}$
^{16}O	$(1.43 \pm 0.28) \times 10^{-1}$	$\mathbf{(1.05 \pm 0.28) \times 10^{-1}}$
^{27}Al	$(1.99 \pm 0.17) \times 10^{-1}$	$\mathbf{(1.59 \pm 0.17) \times 10^{-1}}$
^{48}Ti	$(3.40 \pm 0.27) \times 10^{-1}$	$\mathbf{(2.56 \pm 0.27) \times 10^{-1}}$

Quantitative evaluation was performed using the mean absolute error (MAE), presented in Table 2 for both QMD and LIQMD. It can be observed that the performance of the LIQMD model is better than that of the QMD model, except for the evaluation in ^{10}C.

Based on these results, the challenge for the future in this context is to be able to describe the absolute yield of each fragment, and not only the normalized yield, with more accuracy. In addition, it would be beneficial to compare the simulation results against independent experimental measurements of interest of in-vivo PET.

3.2. Validation of total, differential, and double-differential cross-sections of 95 MeV/u ^{12}c ions incident on thin targets

Fig. 2 illustrates the production cross-section of fragment species with atomic number from 1 to 6, for five different targets (^{1}H, ^{12}C, ^{16}O, ^{27}Al, and ^{48}Ti), with experimental data and simulation results obtained with QMD and LIQMD models. The corresponding MAE values for each target are presented in Table 3. These results reveal that the LIQMD model reproduces data better than QMD model. For the production cross-section, the dominant fragments are the light nuclei (proton, deuteron, etc.), and therefore, the present result indicates an improvement with the LIQMD model for these fragmentations. Moreover, many heavier fragments also show improvement, as depicted in Fig. 2. However, it is worth noting that ^{10}C production overestimates the experimental data for ^{12}C and ^{16}O targets (indicated by red arrows in Fig. 2), which might contribute to the overestimation of this element in positron-emitting radionuclide (see Fig. 1).

Fig. 3 illustrates the differential cross-section of production of ^{1}H, ^{4}He, ^{10}C and ^{11}C fragments, for five different targets (^{1}H, ^{12}C, ^{16}O, ^{27}Al, and ^{48}Ti). The profile of the differential cross-section reveals an obvious difference between the LIQMD and QMD models. Namely, the QMD model tends to predict an emission peak at around 5 ~ 10 degrees, which does not appear in experimental data as pointed out in Dudouet et al. [9], whereas the LIQMD suppresses this formation. Thus, the LIQMD model demonstrates a more accurate reproduction of the cross-section in the forward direction (small angle region) than the QMD model. On the other hand, the overproduction of ^{1}H fragments at angles larger than about 10 degrees is still noticeable even in the LIQMD model. Improvement in this region must be significant for the evaluation of the total yield because ^{1}H fragments are still observed to some extent, even at large angles.

Figs. 4 and 5 illustrate the double-differential cross-section for the same fragments and targets shown in Fig. 3 with respect to the kinetic energy per nucleon of the fragment, for an emission angle of

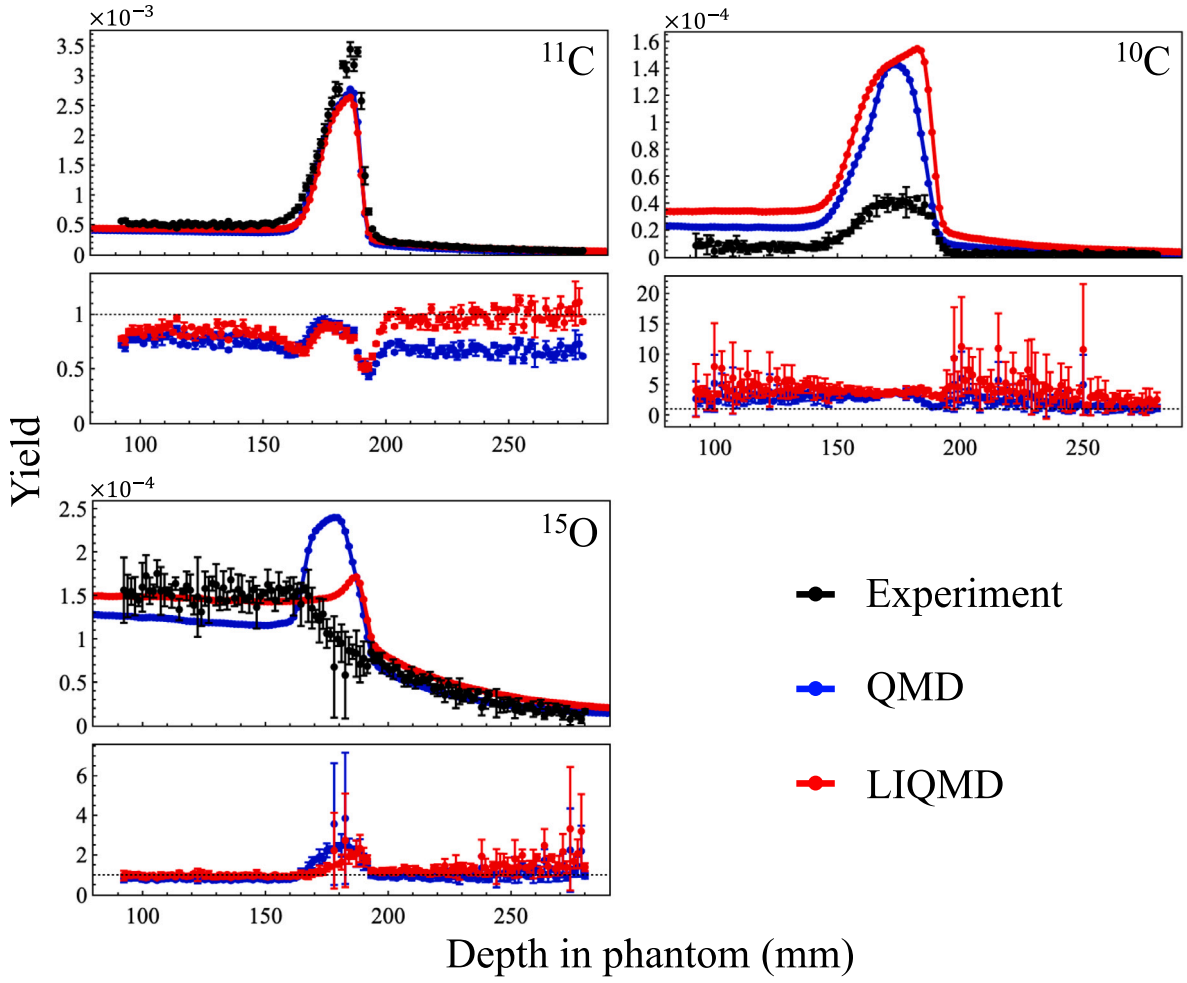

Fig. 1. Yield of three positron-emitting radionuclides (^{11}C, ^{10}C, and ^{15}O), in a PMMA phantom irradiated with a 350 MeV/u ^{12}C ion beam. The experimental data and simulation results obtained with QMD and LIQMD models are represented by black, blue, and red symbols, respectively. The ratio of simulation to experimental values is shown below each panel. (For interpretation of the references to colour in this figure legend, the reader is referred to the web version of this article.)

Table 4
Mean absolute error (MAE) for the differential cross-section and double-differential cross-sections for emission angles of 4 degrees and 15 degrees, corresponding to Figs. 3–5. The **bold** format indicates a smaller MAE, as provided by either the QMD or LIQMD models. If the results of both models are equal to each other, neither is in the bold format.

Target	Fragment	d/Ω		$d^2\sigma/d\Omega dE(4°)$		$d^2\sigma/d\Omega dE(15°)$	
		QMD	LIQMD	QMD	LIQMD	QMD	LIQMD
^{1}H	^{1}H	$\mathbf{(3.25 \pm 2.97) \times 10^{-2}}$	$(5.09 \pm 2.97) \times 10^{-2}$	$\mathbf{(6.65 \pm 1.76) \times 10^{-4}}$	$(1.09 \pm 0.18) \times 10^{-3}$	$\mathbf{(2.03 \pm 0.62) \times 10^{-4}}$	$(3.17 \pm 0.62) \times 10^{-4}$
	^{4}He	$(2.05 \pm 2.43) \times 10^{-1}$	$\mathbf{(2.04 \pm 2.43) \times 10^{-1}}$	$\mathbf{(8.14 \pm 2.43) \times 10^{-3}}$	$(9.23 \pm 2.43) \times 10^{-3}$	$(1.99 \pm 1.67) \times 10^{-4}$	$\mathbf{(1.98 \pm 1.67) \times 10^{-4}}$
	^{10}C	$\mathbf{(3.69 \pm 9.19) \times 10^{-3}}$	$(1.87 \pm 0.92) \times 10^{-2}$	$\mathbf{(5.86 \pm 1.92) \times 10^{-4}}$	$(1.19 \pm 0.19) \times 10^{-3}$	$(4.03 \pm 1.20) \times 10^{-7}$	$(4.03 \pm 1.20) \times 10^{-7}$
	^{11}C	$(7.21 \pm 3.72) \times 10^{-2}$	$\mathbf{(4.34 \pm 3.72) \times 10^{-2}}$	$\mathbf{(5.20 \pm 1.20) \times 10^{-3}}$	$(5.39 \pm 1.20) \times 10^{-3}$	$(7.43 \pm 3.26) \times 10^{-7}$	$(7.43 \pm 3.26) \times 10^{-7}$
^{12}C	^{1}H	$(6.13 \pm 0.33) \times 10^{-1}$	$\mathbf{(3.16 \pm 0.33) \times 10^{-1}}$	$(4.26 \pm 0.17) \times 10^{-3}$	$\mathbf{(2.90 \pm 0.17) \times 10^{-3}}$	$(2.86 \pm 0.06) \times 10^{-3}$	$\mathbf{(1.64 \pm 0.06) \times 10^{-3}}$
	^{4}He	$(4.92 \pm 0.92) \times 10^{-1}$	$\mathbf{(2.47 \pm 0.92) \times 10^{-1}}$	$(1.98 \pm 0.18) \times 10^{-2}$	$\mathbf{(1.23 \pm 0.18) \times 10^{-2}}$	$(2.98 \pm 0.09) \times 10^{-3}$	$\mathbf{(1.70 \pm 0.09) \times 10^{-3}}$
	^{10}C	$(1.68 \pm 0.25) \times 10^{-2}$	$\mathbf{(1.39 \pm 0.25) \times 10^{-2}}$	$\mathbf{(6.73 \pm 1.34) \times 10^{-4}}$	$(1.25 \pm 0.13) \times 10^{-3}$	$(2.38 \pm 0.12) \times 10^{-6}$	$\mathbf{(1.87 \pm 0.11) \times 10^{-6}}$
	^{11}C	$(7.00 \pm 1.01) \times 10^{-2}$	$\mathbf{(1.93 \pm 1.01) \times 10^{-2}}$	$\mathbf{(6.37 \pm 0.57) \times 10^{-3}}$	$(6.62 \pm 0.57) \times 10^{-3}$	$(2.30 \pm 0.17) \times 10^{-6}$	$\mathbf{(2.25 \pm 0.17) \times 10^{-6}}$
^{16}O	^{1}H	$(6.96 \pm 0.78) \times 10^{-1}$	$\mathbf{(3.76 \pm 0.78) \times 10^{-1}}$	$(4.75 \pm 0.40) \times 10^{-3}$	$\mathbf{(3.30 \pm 0.40) \times 10^{-3}}$	$(3.41 \pm 0.15) \times 10^{-3}$	$\mathbf{(1.98 \pm 0.15) \times 10^{-3}}$
	^{4}He	$(6.10 \pm 1.93) \times 10^{-1}$	$\mathbf{(2.92 \pm 1.93) \times 10^{-1}}$	$(2.45 \pm 0.36) \times 10^{-2}$	$\mathbf{(1.48 \pm 0.36) \times 10^{-2}}$	$(4.20 \pm 0.21) \times 10^{-3}$	$\mathbf{(2.13 \pm 0.21) \times 10^{-3}}$
	^{10}C	$(1.80 \pm 0.44) \times 10^{-2}$	$\mathbf{(1.29 \pm 0.44) \times 10^{-2}}$	$\mathbf{(8.40 \pm 2.51) \times 10^{-4}}$	$(1.00 \pm 0.25) \times 10^{-3}$	$(7.90 \pm 0.89) \times 10^{-6}$	$\mathbf{(5.25 \pm 0.89) \times 10^{-6}}$
	^{11}C	$(7.21 \pm 1.77) \times 10^{-2}$	$\mathbf{(2.09 \pm 1.77) \times 10^{-2}}$	$(8.87 \pm 1.20) \times 10^{-3}$	$\mathbf{(7.92 \pm 1.20) \times 10^{-3}}$	$(7.63 \pm 0.59) \times 10^{-6}$	$\mathbf{(4.91 \pm 0.58) \times 10^{-6}}$
^{27}Al	^{1}H	$(8.85 \pm 0.49) \times 10^{-1}$	$\mathbf{(4.73 \pm 0.49) \times 10^{-1}}$	$(5.47 \pm 0.25) \times 10^{-3}$	$\mathbf{(4.18 \pm 0.25) \times 10^{-3}}$	$(4.34 \pm 0.10) \times 10^{-3}$	$\mathbf{(2.44 \pm 0.10) \times 10^{-3}}$
	^{4}He	$(8.43 \pm 1.16) \times 10^{-1}$	$\mathbf{(4.00 \pm 1.16) \times 10^{-1}}$	$(3.62 \pm 0.23) \times 10^{-2}$	$\mathbf{(2.08 \pm 0.23) \times 10^{-2}}$	$(6.97 \pm 0.13) \times 10^{-3}$	$\mathbf{(3.29 \pm 0.13) \times 10^{-3}}$
	^{10}C	$(1.74 \pm 0.22) \times 10^{-2}$	$\mathbf{(1.11 \pm 0.22) \times 10^{-2}}$	$\mathbf{(7.83 \pm 1.24) \times 10^{-4}}$	$(8.04 \pm 1.24) \times 10^{-4}$	$(1.93 \pm 0.07) \times 10^{-5}$	$\mathbf{(9.78 \pm 0.68) \times 10^{-6}}$
	^{11}C	$(6.80 \pm 0.83) \times 10^{-2}$	$\mathbf{(3.56 \pm 0.83) \times 10^{-2}}$	$(1.11 \pm 0.06) \times 10^{-2}$	$\mathbf{(8.54 \pm 0.59) \times 10^{-3}}$	$(7.87 \pm 0.07) \times 10^{-5}$	$\mathbf{(2.17 \pm 0.05) \times 10^{-5}}$
^{48}Ti	^{1}H	1.17 ± 0.06	$\mathbf{(5.88 \pm 0.63) \times 10^{-1}}$	$(6.10 \pm 0.30) \times 10^{-3}$	$\mathbf{(5.02 \pm 0.30) \times 10^{-3}}$	$(5.51 \pm 0.13) \times 10^{-3}$	$\mathbf{(2.98 \pm 0.13) \times 10^{-3}}$
	^{4}He	1.04 ± 0.14	$\mathbf{(5.18 \pm 1.36) \times 10^{-1}}$	$(4.80 \pm 0.30) \times 10^{-2}$	$\mathbf{(2.77 \pm 0.30) \times 10^{-2}}$	$(1.01 \pm 0.02) \times 10^{-2}$	$\mathbf{(4.61 \pm 0.17) \times 10^{-3}}$
	^{10}C	$(2.02 \pm 0.25) \times 10^{-2}$	$\mathbf{(1.16 \pm 0.25) \times 10^{-2}}$	$\mathbf{(8.80 \pm 1.66) \times 10^{-4}}$	$(9.71 \pm 1.66) \times 10^{-4}$	$(1.16 \pm 0.01) \times 10^{-4}$	$\mathbf{(3.55 \pm 0.05) \times 10^{-5}}$
	^{11}C	$(1.08 \pm 0.09) \times 10^{-1}$	$\mathbf{(5.36 \pm 0.87) \times 10^{-2}}$	$(1.78 \pm 0.07) \times 10^{-2}$	$\mathbf{(1.28 \pm 0.07) \times 10^{-2}}$	$(1.98 \pm 0.01) \times 10^{-4}$	$\mathbf{(4.84 \pm 0.07) \times 10^{-5}}$

4 and 15 degrees, respectively. The result of 4 degrees is shown as representative of the forward direction and 15 degrees is shown as representative of the larger angle direction. In particular, in the case of the energy distribution at an emission angle of 4 degrees, the yield of ^{1}H fragments with energy below 95 MeV (incident kinetic energy/nucleon) is significantly improved for all targets except for the ^{1}H target. For

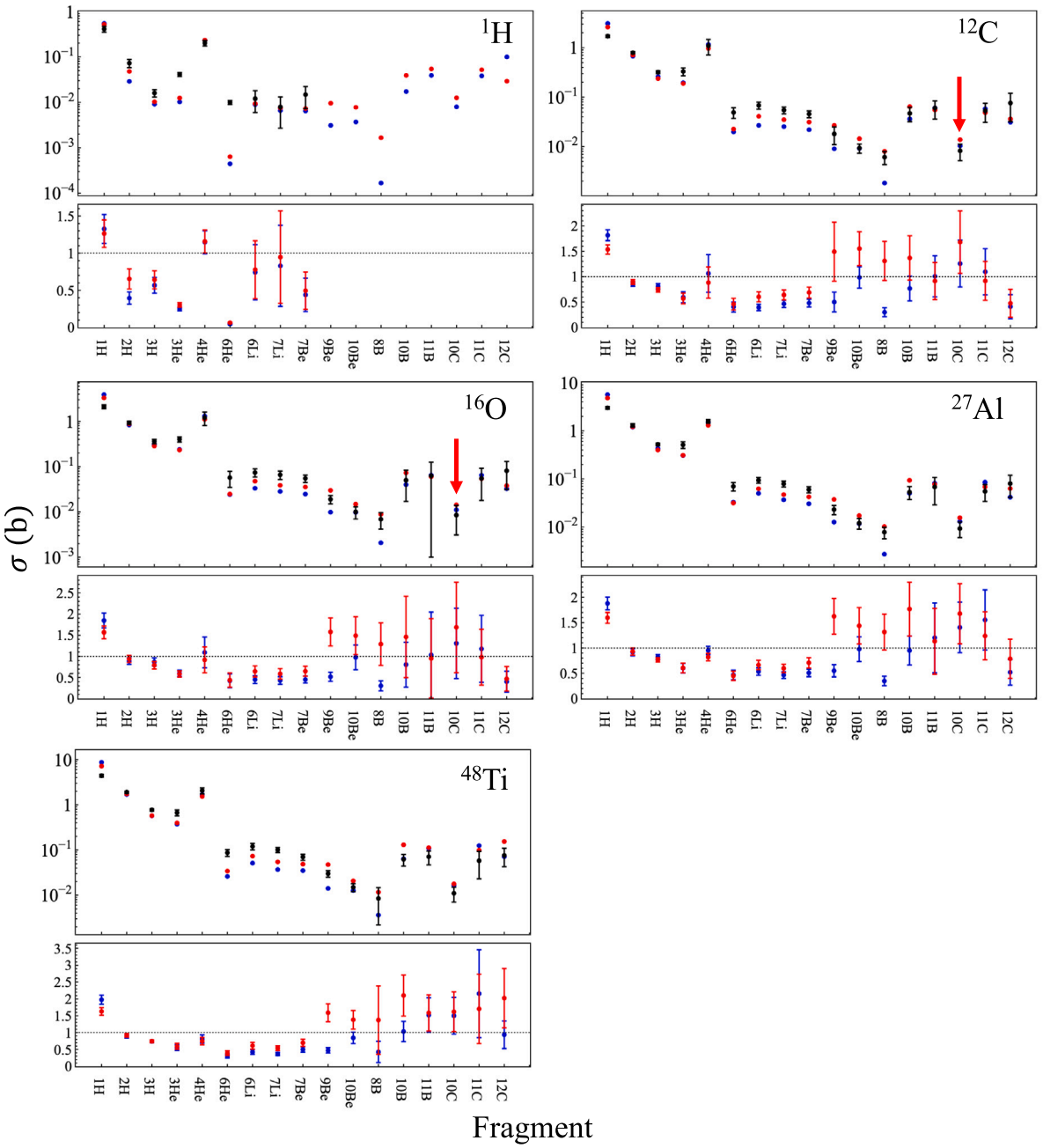

Fig. 2. Total cross-section of production of different fragments for five different targets (^{1}H, ^{12}C, ^{16}O, ^{27}Al, and ^{48}Ti). The experimental data and simulation results obtained with QMD and LIQMD models are represented by black, blue, and red circles with error bars, respectively. In almost all simulations, the standard errors are small enough to be hidden by the markers. Notably, for the ^{1}H target, there are no experimental data for fragments heavier than ^{9}Be. The ratio of simulation to experimental values is shown below each panel. The red arrows indicate the ^{10}C fragment in ^{12}C and ^{16}O targets, which are components of a PMMA phantom. (For interpretation of the references to colour in this figure legend, the reader is referred to the web version of this article.)

the other fragments, there is no significant improvement. The trend is not as pronounced at 15 degrees as at 4 degrees. In particular, both QMD and LIQMD are not able to reproduce the yields of fragments with kinetic energies higher than the energy of the incident beam (95 MeV/u), and further improvement is needed.

In the experiment conducted by Dudouet et al. [25], seventeen different fragments were measured for each of the five targets, resulting in a total of eighty five differential cross-sections. Additionally, in the double-differential cross-section, data exist for each measured angle. Analysing all the data provided by Ref. [25], we found that the LIQMD model quantitatively improves MAE by 82.4% (70/85) and 74.1% (1225/1654), in terms of differential and double-differential cross-sections, respectively (See supplemental information). For the fragmentation of almost all targets considered in this study, Table 3 demonstrates that the LIQMD model agrees with the experimental measurements better than the QMD in the total cross-sections. However, for the ^{1}H target, both the angular and energy distributions obtained with the LIQMD model were not reproduced better than by the QMD model (see Table 4).

4. Discussion

In this work, we evaluated the LIQMD model, newly developed in the Geant4 hadronic physics for hadron therapy, against experimental data in terms of positron-emitting radionuclides yields and of fragment production cross-sections in thin targets. Overall, the LIQMD model

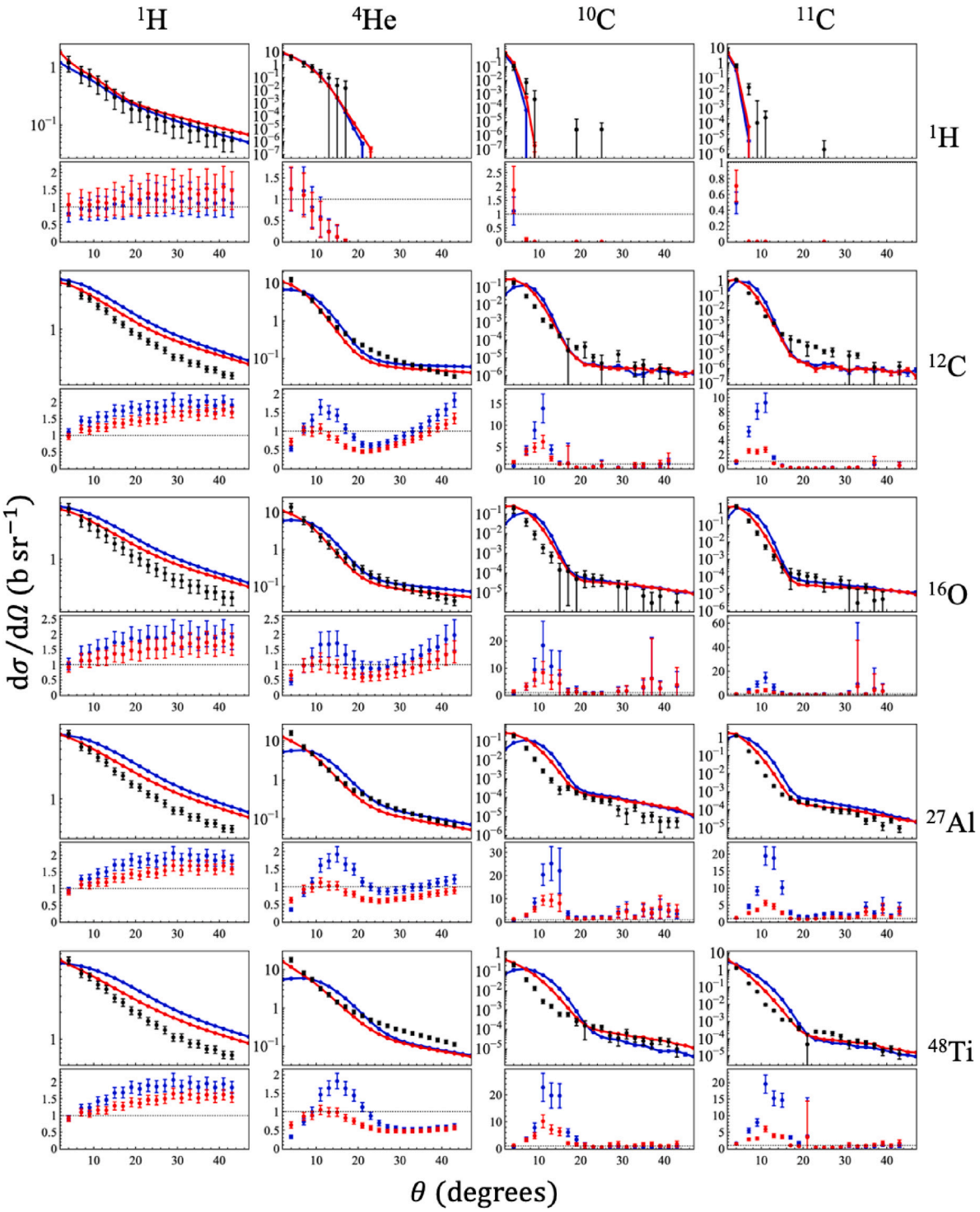

Fig. 3. Differential cross-section of ^{1}H, ^{4}He, ^{10}C and ^{11}C fragments for five targets (^{1}H, ^{12}C, ^{16}O, ^{27}Al, and ^{48}Ti) as a function of the emission angle. The experimental data and the simulation results obtained with QMD and LIQMD models are indicated by black, blue, and red symbols, respectively. The ratio of simulation to experimental values is shown below each panel. (For interpretation of the references to colour in this figure legend, the reader is referred to the web version of this article.)

can well reproduce both experimental datasets, when compared to the Geant4 default QMD model. Particularly noteworthy is the normalized distribution (profile shape) of positron-emitting radionuclides, which has been effectively described by the LIQMD model (see Appendix). This improvement is attributed to the fact that the LIQMD model significantly enhances angular emission of fragments in the forward direction, as depicted in Fig. 3. The corresponding kinetic energy distributions for ^{10}C and ^{11}C fragments in ^{1}H, ^{12}C, and ^{16}O targets constituting PMMA are also in reasonable agreement with the experimental data (as seen in Fig. 4), partly supporting the presented results. However, for absolute positron emission yield comparison, a substantial discrepancy still exists, particularly in terms of ^{10}C yield (see Fig. 1). This indicates an overestimation of ^{10}C production in the LIQMD calculation. This overestimation is also true for the QMD calculation. The production of ^{11}C and ^{10}C is considered to be a one or two neutron knockout phenomena from ^{12}C, and theoretical calculations of this phenomenon have also been made, and the importance of nuclear

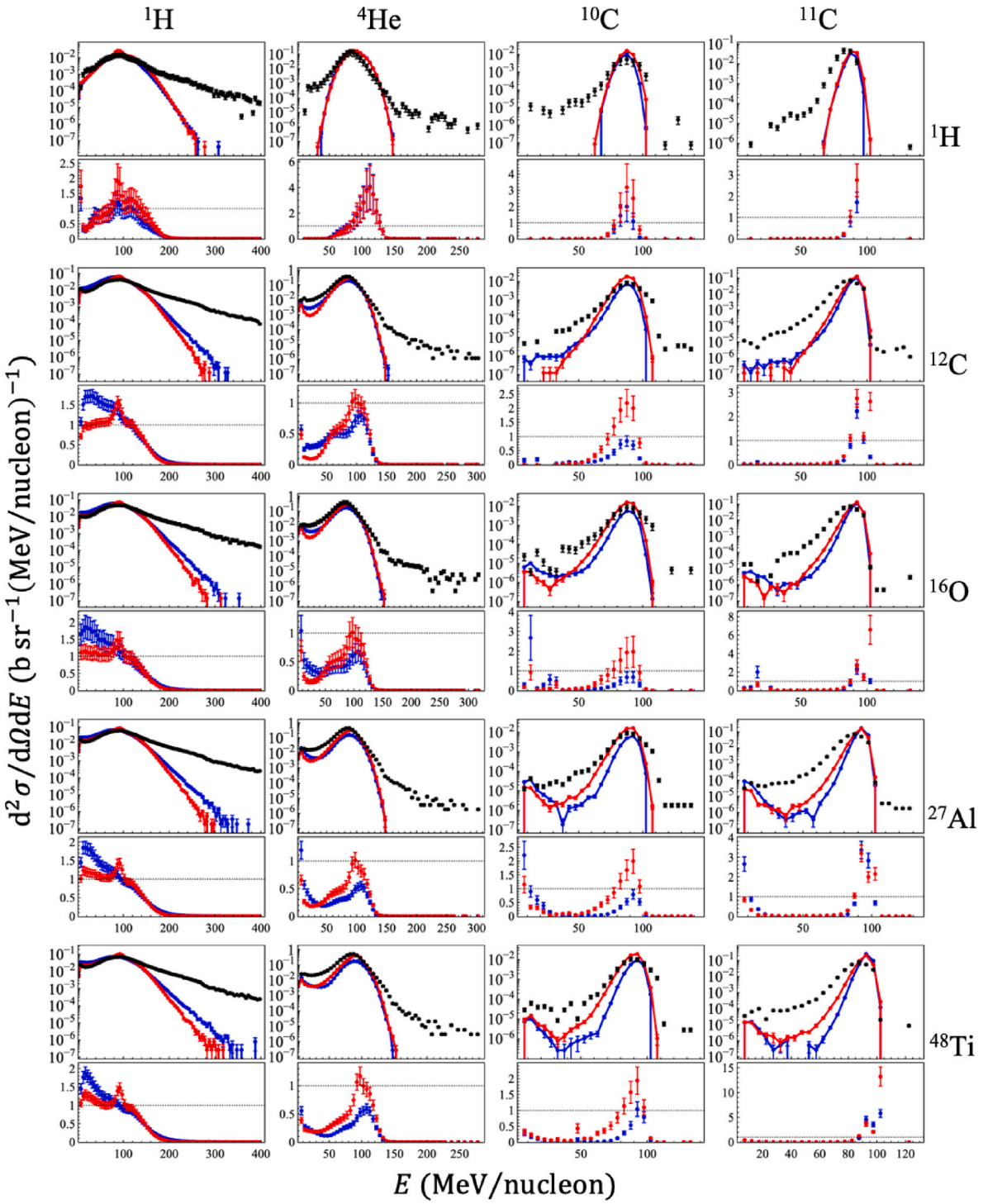

Fig. 4. Double-differential cross-section of ^{1}H, ^{4}He, ^{10}C and ^{11}C fragments for five targets (^{1}H, ^{12}C, ^{16}O, ^{27}Al, and ^{48}Ti) at an emission angle of 4 degrees as a function of the kinetic energy per nucleon of the fragment. The experimental data and the simulation results obtained with QMD and LIQMD are indicated by black, blue, and red, respectively. The ratio of simulation to experimental values is shown below each panel. (For interpretation of the references to colour in this figure legend, the reader is referred to the web version of this article.)

structure is discussed [31–33]. This observation aligns with the results of the production cross-section for ^{10}C fragment yield, as illustrated in Fig. 2. To accurately reproduce the distribution of positron emitters, further development of the model is necessary. For this purpose, it would be beneficial to compare the model with other experimental data of different incident energies, as well as the cross–section data for a wider energy range.

Concerning the profile shape of radionuclides, the peak around 180 mm depth in the ^{15}O distribution, as depicted in Fig. 1 produced by the QMD model, becomes less prominent in the case of the LIQMD model, with its profile aligning more closely with the experimental trend. Although the cause of this improvement is not definitively determined, it is likely attributed to the fact that the LIQMD model permits the use of a lower threshold for the projectile (incident) kinetic

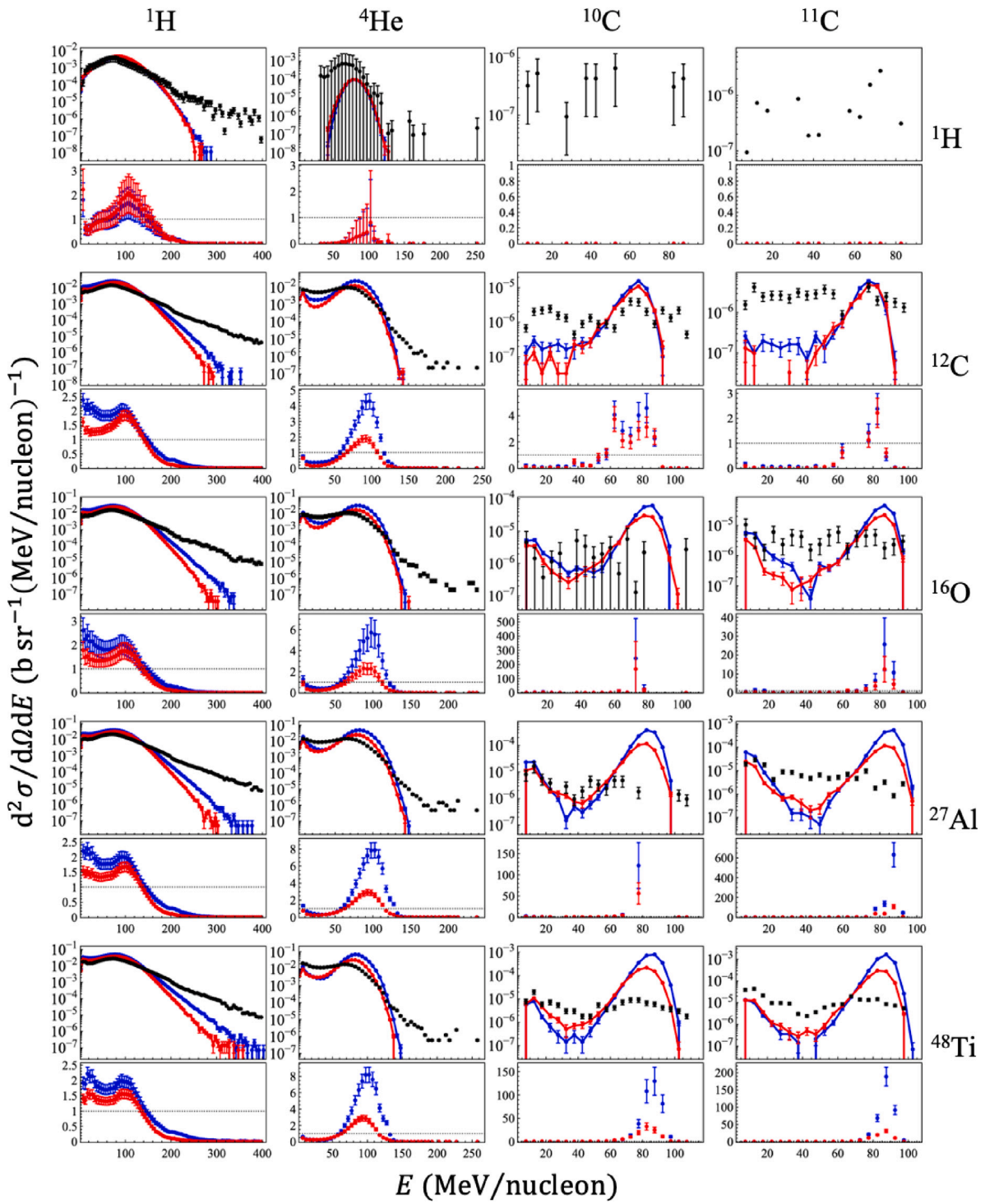

Fig. 5. Double-differential cross-section of ^{1}H, ^{4}He, ^{10}C and ^{11}C fragments for five targets (^{1}H, ^{12}C, ^{16}O, ^{27}Al, and ^{48}Ti) at an emission angle of 15 degrees, as a function of the kinetic energy per nucleon of the fragment. The experimental data and simulation results obtained with QMD and LIQMD are indicated by black, blue, and red symbols, respectively. As it can be seen in Fig. 3, the ^{10}C and ^{11}C fragments in the case of an ^{1}H target were not produced at this angle in our simulations. The ratio of simulation to experimental values is shown below each panel. (For interpretation of the references to colour in this figure legend, the reader is referred to the web version of this article.)

energy. The physics constructor called `G4IonQMDPhysics` was used in this work to select the QMD model, as commonly done in Geant4 (the models used to describe the hadron inelastic process are indicated as *Hadron Inelastic* in Table 1). A new constructor was created in Geant4 11.2 to select the LIQMD model (referred as *Hadron Inelastic** in Table 1). The QMD constructor is usually set to switch from the QMD to the BIC when the kinetic energy of the projectile is below 100 MeV/u, whereas the LIQMD model was allowed down to 30 MeV/u, serving as the threshold energy for transitioning to the BIC model. The QMD model, providing a more accurate description of the interaction among the projectile and target nucleons than the BIC, is expected to better reproduce experimental data. The observed difference in the ^{15}O distribution may be regarded as one of the accomplishments resulting from this fact.

Finally, we have to acknowledge the limitations of the QMD and LIQMD models when calculating positron-emitting radionuclides yields

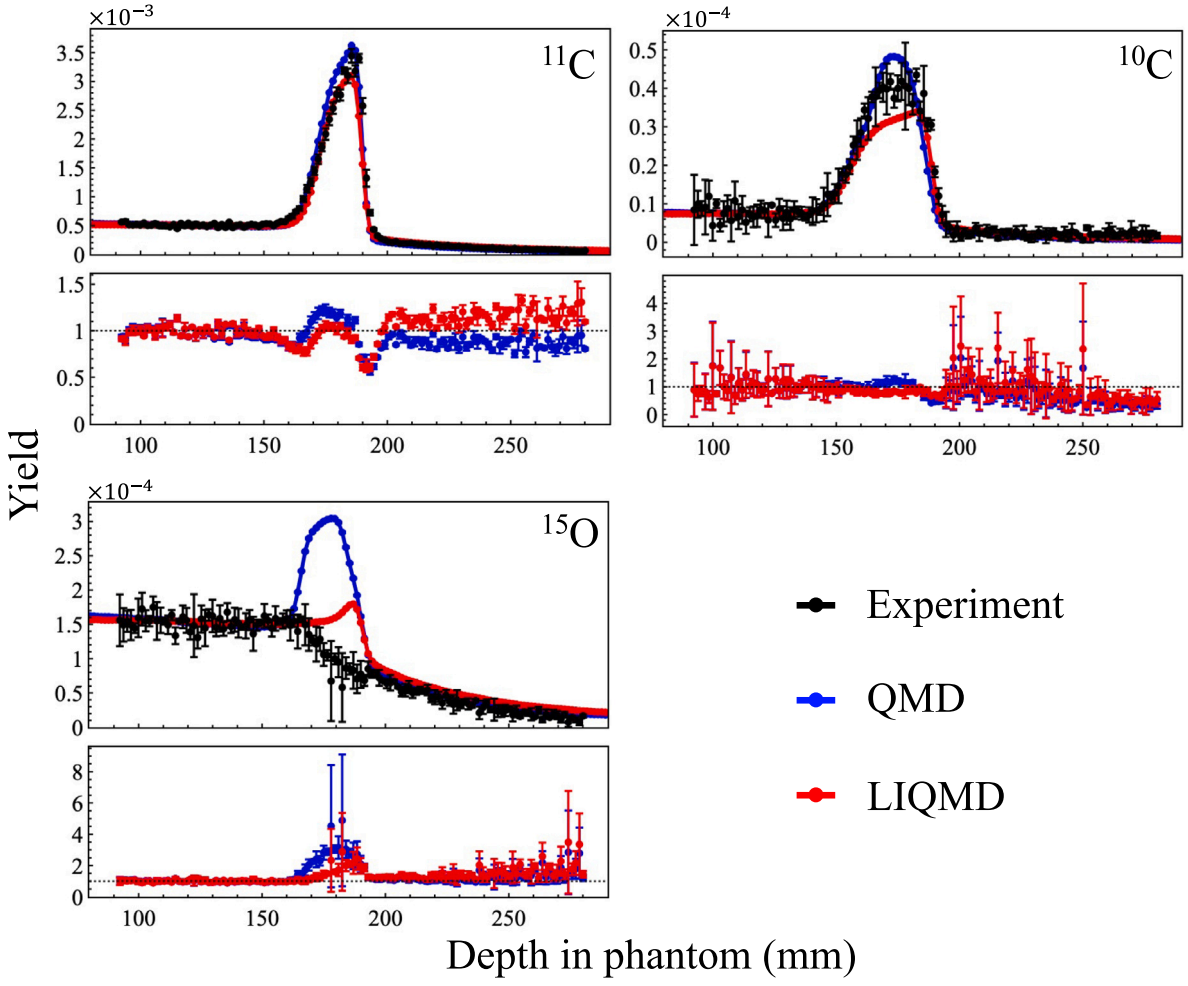

Fig. 6. Normalized yield of three positron-emitting radionuclides (^{11}C, ^{10}C, and ^{15}O), in a PMMA phantom irradiated with a 350 MeV/u ^{12}C ion beam. The experimental data and simulation results obtained with QMD and LIQMD models are represented by black, blue, and red symbols, respectively. The yield distributions normalized to the mean value of the experimental data at the entrance of the phantom, between 100 mm and 130 mm. The ratio of simulation to experimental values is shown below each panel. (For interpretation of the references to colour in this figure legend, the reader is referred to the web version of this article.)

and inelastic cross-section. In simulating nucleus–nucleus collisions, the impact parameter (commonly referred to as b) is initially sampled within a specified range. In both QMD and LIQMD models in Geant4, the impact parameter is determined by multiplying $b_{env}\sqrt{\sigma_{inel}/\pi}$ with the square root of a uniform distribution (within the range [0,1]). Here, σ_{inel} denotes the inelastic cross-section provided by the theoretical model (the Glauber–Gribov model [29,30] is utilized in Geant4). The enhancement (envelope) factor b_{env} is set equal to a constant value of 1.05, which has never been concretely justified in use of inelastic collision. This factor may depend on the projectile, target, and/or the kinetic energy in the collision, as the reproducibility of σ_{inel} varies with these parameters. For instance, when the theoretical inelastic cross-section underestimates the experiment, a larger b_{env} may be useful to augment the peripheral reaction in fragmentation. Altering the number of peripheral collisions significantly influences fragment yields, such as the production of ^{10}C and ^{11}C. Therefore, further investigation into an appropriate b_{env} may be necessary. It is also crucial to note that an accurate inelastic cross-section is essential for reproducing absolute yields, since the QMD models solely simulate nuclear fragmentation, implying that they are responsible not for absolute production but for the relative production of fragments.

5. Conclusion

In this paper, we benchmarked the LIQMD model, specially developed for hadron therapy simulation applications, using experimental data on the distribution of positron-emitting radionuclides and 95 MeV/n ^{12}C cross-section data for ^{1}H, ^{12}C, ^{16}O, ^{27}Al, and ^{48}Ti targets. These targets involve the same elements or elements with similar mass numbers to those in human anatomies. The profile shape of positron-emitting radionuclides in the LIQMD model can better reproduce experimental data compared to the default Geant4 QMD model. However, there still exists a difference between Geant4 simulations and experimental data in terms of absolute positron-emitting fragment yields, which is consistent with the results of the 95 MeV/n ^{12}C cross-section test. The LIQMD model significantly improves the prediction of the 95 MeV/n ^{12}C differential and double-differential cross-sections of fragments in all targets under study, except for the ^{1}H target. This improvement allows to simulate more accurate simulation of fragmentation processes in carbon ion therapy. The LIQMD model has been recently incorporated in Geant4 11.2. Research to further improve this model is ongoing. In the near future, we plan to expand the model's scope and confirm its usefulness not only in hadron therapy but also in the study of heavy particles and high-energy phenomena, with implications for space science and engineering.

Declaration of competing interest

None

Acknowledgements

This work was supported by JST, Japan, the establishment of university fellowships towards the creation of science technology innovation, Grant Number JPMJFS2130 and JSPS KAKENHI, Japan, Grant No. 23K07084.

Appendix

In this appendix, we present the distribution of positron-emitting radionuclide production along the beam direction in a PMMA phantom irradiated with 350 MeV/u ^{12}C ions in Fig. 6, in order to compare the profile shapes between the theoretical simulation and experimental data. The yield of each fragment is normalized to align the simulation with the experimental results within the plateau region (100-130 mm). The corresponding quantitative evaluation using the mean absolute error (MAE) are presented in Table 5.

Table 5
Mean absolute error (MAE) of the positron-emitting radionuclides production for normalized yields (Fig. 6). The **bold** format indicates a smaller MAE, as provided by either the QMD or the LIQMD model.

Nuclide	QMD	LIQMD
^{11}C	$(7.33 \pm 0.36) \times 10^{-5}$	$\mathbf{(5.99 \pm 0.36) \times 10^{-5}}$
^{10}C	$\mathbf{(2.05 \pm 0.26) \times 10^{-6}}$	$(2.13 \pm 0.26) \times 10^{-6}$
^{15}O	$(2.91 \pm 0.14) \times 10^{-5}$	$\mathbf{(1.70 \pm 0.14) \times 10^{-5}}$

References

[1] Agostinelli S, et al. Geant4—a simulation toolkit. Nucl Instrum Methods Phys Res A 2003;506:250–303. http://dx.doi.org/10.1016/S0168-9002(03)01368-8.
[2] Allison J, et al. Geant4 developments and applications. IEEE Trans Nucl Sci 2006;53:270–8. http://dx.doi.org/10.1109/TNS.2006.869826.
[3] Allison J, et al. Recent developments in Geant4. Nucl Instrum Methods Phys Res A 2016;835:186–225. http://dx.doi.org/10.1016/j.nima.2016.06.125.
[4] Muraro S, Battistoni G, Kraan AC. Challenges in Monte Carlo simulations as clinical and research tool in particle therapy: A review. Front Phys 2020;8.
[5] Arce P, et al. Report on G4-med, a Geant4 benchmarking system for medical physics applications developed by the Geant4 medical simulation benchmarking group. Med Phys 2021;48(1):19–56.
[6] Folger Gunter, et al. The binary cascade. Eur Phys J A 2004;21(3):407–17.
[7] Boudard Alain, et al. New potentialities of the Liège intranuclear cascade (INCL) model for reactions induced by nucleons and light charged particles. 2012, arXiv:1210.3498.
[8] Mancusi Davide, et al. Extension of the Liège Intranuclear-Cascade model to reactions induced by light nuclei. 2014, arXiv:1407.7755.
[9] Dudouet J, et al. Benchmarking geant4 nuclear models for hadron therapy with 95 MeV/nucleon carbon ions. Phys Rev C 2014;89(5):054616.
[10] Bolst David, et al. Validation of Geant4 fragmentation for heavy ion therapy. Nucl Instrum Methods Phys Res A 2017;869:68–75.
[11] Chacon Andrew, et al. Comparative study of alternative Geant4 hadronic ion inelastic physics models for prediction of positron-emitting radionuclide production in carbon and oxygen ion therapy. Phys Med Biol 2019;64(15):155014.
[12] Sato Yoshi-Hide, et al. Development of a more accurate Geant4 quantum molecular dynamics model for hadron therapy. Phys Med Biol 2022;67(22).
[13] Chacon Andrew, et al. A quantitative assessment of Geant4 for predicting the yield and distribution of positron-emitting fragments in ion beam therapy. Phys Med Biol 2024;69(12):125015.
[14] Kosaki K, Ecker S, Habermehl D. Comparison of intensity modulated radiotherapy (IMRT) with intensity modulated particle therapy (IMPT) using fixed beams or an ion gantry for the treatment of patients with skull base meningiomas. Radiat Oncol 2012;7(3):44. http://dx.doi.org/10.1186/1748-717X-7-44.
[15] L. Wang, et al. Intensity-modulated carbon-ion radiation therapy versus intensity-modulated photon-based radiation therapy in locally recurrent nasopharyngeal carcinoma: a dosimetric comparison. Cancer Manag Res 2019;16(11):7767–77. http://dx.doi.org/10.2147/CMAR.S205421.
[16] Paganetti Harald. Range uncertainties in proton therapy and the role of Monte Carlo simulations. Phys Med Biol 2012;57(11):R99–117.
[17] Sokol Olga, et al. Potential benefits of using radioactive ion beams for range margin reduction in carbon ion therapy. Sci Rep 2022;12(1):21792.
[18] Zhu Xuping, El Fakhri Georges. Proton therapy verification with PET imaging. Theranostics 2013;3(10):731–40.
[19] Kraan AC, et al. Proton range monitoring with in-beam PET: Monte Carlo activity predictions and comparison with cyclotron data. Phys Med 2014;30(5):559–69.
[20] Geant4 Collaboration. Physics reference manual documentation release 10.7. 2020, p. 374, https://geant4-userdoc.web.cern.ch/usersguides/physicsreferencemanual/backupversions/v10.7/fo/physicsreferencemanual.pdf.
[21] Mancusi Davide, et al. Stability of nuclei in peripheral collisions in the JAERI quantum molecular dynamics model. Phys Rev C 2009;79(1):014614.
[22] Niita Koji, et al. Analysis of the (N, xN′) reactions by quantum molecular dynamics plus statistical decay model. Phys Rev C 1995;52(5):2620.
[23] Niita Koji, et al.
[24] Maruyama Toshiki, Niita Koji, Iwamoto Akira. Extension of quantum molecular dynamics and its application to heavy-ion collisions. Phys Rev C 1996;53(1):297.
[25] Dudouet J, et al. Double-differential fragmentation cross-section measurements of 95 MeV/nucleon 12 C beams on thin targets for hadron therapy. Phys Rev C 2013;88(2):024606.
[26] Akamatsu Go, et al. Performance evaluation of a whole-body prototype PET scanner with four-layer DOI detectors. Phys Med Biol 2019;64(9):095014. http://dx.doi.org/10.1088/1361-6560/ab18b2.
[27] Panin Vladimir Y, et al. Fully 3-D PET reconstruction with system matrix derived from point source measurements. IEEE Trans Med Imaging 2006;25(7):907–21.
[28] Dudouet J, et al. Zero-degree measurements of C 12 fragmentation at 95 MeV/nucleon on thin targets. Phys Rev C Nucl Phys 2014;89(6):064615.
[29] Grichine VM. A simple model for integral hadron–nucleus and nucleus–nucleus cross-sections. Nucl Instrum Methods Phys Res B 2009;267(14):2460–2.
[30] Grichine VM. A simplified Glauber model for hadron–nucleus cross sections. Eur Phys J C 2009;62(2):399–404.
[31] Simpson EC, Tostevin JA. Two-nucleon correlation effects in knockout reactions from 12C. 2010, arXiv:1012.1543.
[32] Simpson EC, et al. Microscopic two-nucleon overlaps and knockout reactions from ^{12}C. 2012, arXiv:1207.5695.
[33] Simpson EC. Production of the PET isotope 11C in hadron therapy via neutron knockout. Phys Med 2016;32(12):1813–8.